Journal of
Food Chemistry & Nanotechnology

https://doi.org/10.17756/jfcn.2025-s2-001

Research Article

Open Access

Investigation on Structural and Elastic Properties of Nickel Ferrite Nanoparticles Synthesized via Green Route

Poorwang K Bhatt, Payalkumari M Savaliya, Shyam R Ajudiya, Ashish R Tanna and Harshal B Desai*

Department of Physics, School of Science, RK University, Gujarat, India

***Correspondence to:**
Harshal B Desai
Department of Physics,
School of Science,
RK University,
Gujarat, India.
E-mail: harshal.desai@rku.ac.in

Received: April 25, 2025
Accepted: June 26, 2025
Published: July 02, 2025

Citation: Bhatt PK, Savaliya PM, Ajudiya SR, Tanna AR, Desai HB. 2025. Investigation on Structural and Elastic Properties of Nickel Ferrite Nanoparticles Synthesized via Green Route. *J Food Chem Nanotechnol* 11(S2): S1-S9.

Copyright: © 2025 Bhatt et al. This is an Open Access article distributed under the terms of the Creative Commons Attribution 4.0 International License (CC-BY) (https://creativecommons.org/licenses/by/4.0/) which permits commercial use, including reproduction, adaptation, and distribution of the article provided the original author and source are credited.

Published by United Scientific Group

Abstract

Nickel ferrite nanoparticles are synthesized using *Mangifera Indica* pulp (mango pulp) as a fuel in the self-combustion method. The green synthesis route is inexpensive, eco-friendly, and easily scalable for producing large quantities of solid materials. Fruit pulp-mediated nickel ferrite nanoparticles were characterized using energy dispersive X-ray (EDX), scanning electron microscopy (SEM), X-ray diffraction (XRD), fourier transform infrared spectroscopy (FTIR), and transmission electron microscopy (TEM) techniques. The EDX confirms that the prepared nickel ferrite nanoparticles have no impurity, and the specimen has nickel, iron, and oxygen, and they are in good proportion with experimental and theoretical values of molar weight. SEM revealed the porous structure of the prepared nanoparticles. Various structural properties are investigated using the XRD analysis of the specimen, i.e., crystallite size, crystal structure, X-ray density, bulk density, porosity, surface area, dislocation factor, cation distribution, and other parameters. Tetrahedral and octahedral force constants, and elastic properties of synthesized nanoparticles are investigated using FTIR analysis, i.e., stiffness constant, young's modulus, rigidity modulus, and bulk modulus. The average particle size is calculated using TEM analysis of synthesized nanoparticles.

Keywords

Spinel, Green synthesis, *Mangifera Indica*, X-ray diffraction, Cation distribution, Fourier transform infrared spectroscopy

Introduction

Normal spinel structure has a cubic structure and has the chemical formula MB_2O_4 (MFe_2O_4). A occupies tetrahedral and B occupies octahedral lattice sites in the crystal. The spinel MFe_2O_4 has a structural formula $[M^{2+}][Fe^{3+}]_2O_4$, where $[Fe^{3+}]$ ions are on the B site, i.e., octahedral site, and $[M^{2+}]$ ions are on the A site, i.e., tetrahedral site. Inverse spinel has the structure $Fe^{3+}[M^{2+}Fe^{3+}]O_4^{2-}$ in which M^{2+} is on octahedral sites (B sites) and Fe^{3+} ions are on tetrahedral (A sites) and octahedral (B sites) sites. $(M_{1-x}Fe_x)[Fe_{2-x}M_x]O_4$ is the structure formula for mixed spinel ferrite in which M^{2+} and Fe^{3+} ions are randomly distributed over both A sites and B sites [1, 2]. Spinel ferrites have a total of 56 in arrangement with a cubic structure, in which out of 64 cations on A sites, 24 cations occupy 8 sites, and 16 out of 32 cations are occupied on B sites, and oxygen anions are 32 [3, 4]. It is well known that ferrites have various applications due to their magnetic properties. It can be used in quality filter circuits, wide-band transformers, drug delivery, gas sensing devices, electromagnet and microwave, photocatalytic, wastewater treatment, biomedical, humidity sensors, etc. [1].

Sarala et al. [5] prepared nickel ferrite nanoparticles via a green synthesis method using different volumes, specifically 10 ml and 20 ml of leaf extract from

Terminalla catappa, and named the samples NF1 and NF2, respectively. The crystallite size is found to decrease from 11.97 nm to 8.01 nm as increased the leaf extract. XRD, FTIR, EDX analysis, selected area electron diffraction (SAED), TEM, and high-resolution TEM (HRTEM) characterization were done to analyze the sample. With the comparison between sample NF1 and NF2, the anticancer activity for MCF-7 cell lines (a cell line for breast cancer) showed the best result of cytotoxicity effect for sample NF1 with the lowest cell viability of 24.92% at 500 µg/ml [5]. Nano-crystalline nickel ferrite using the extract of ginger, prepared by Patil et al. [6] thermogravimetric analysis (TGA), XRD, FTIR and ultraviolet-visible (UV - Vis.) characterization were done for the specimen. The crystallite size of the prepared sample was 26 nm, which was derived using the Debye-Scherrer formula. Moreover, structural and physical properties have been studied from the results of characterization [6]. Nanoparticles of nickel ferrite were synthesized using rosemary extract by Alijani et al. [7]. Sample characterized by XRD, HRTEM, field emission SEM (FESEM), X-ray photoelectron spectroscopy (XPS), FTIR, EDX analysis, vibrating sample magnetometry (VSM), and ED spectrometer (EDS). Prepared samples were studied for an anticancer activity [7]. Kulkarni et al. [8] used the green synthesis method and the sol-gel auto combustion method to prepare nickel ferrite nanoparticles. In which clove (*Syzygium aromaticum*) was used as a green fuel agent, and citric acid as a chemical fuel agent were used to synthesize nickel ferrite nanoparticles. For both samples, the crystallite size was found to be 24 nm and 26 nm for the green and chemical routes, respectively. Furthermore, X-ray density, ionic radii, bulk density, and volume of a unit cell of prepared samples were compared [8]. *Saccharum munja* as a raw biomass material and using a bio-genetically method, nickel ferrite nanoparticles were synthesized by Din et al. [9]. The sample was analyzed by UV-VIS and FTIR characterization techniques. Study confirms that the prepared specimen with *S. munja* can be used for the production of high-yield biofuel [9]. Udhaya and Meena [10] synthesized nickel ferrite nanoparticles from albumen (egg white) via the self-combustion method. Material's physico-chemical properties were studied using the characterization powder XRD (PXRD), FTIR, EDX, FESEM, photoluminescence e, and VSM. Magnetic parameters and dielectric properties were studied for the nickel ferrite, and the specimen's particle size ranges between 23 - 47 nm. Also, the absorption peaks were observed at 419 cm^{-1} and 589 cm^{-1} from FTIR. FESEM shows the agglomeration. Structural, morphology, optical, elemental, and dielectric properties have been studied, and magnetic parameters like coercivity, retentivity, and magnetic moment were also calculated for the prepared specimen [10]. Pristine and Mg-doped nickel ferrite nanoparticles were synthesized from aloe vera gel via the green sol-gel method by Nadumane et al. [11]. Samples were characterized by PXRD, SEM, TEM, and HRTEM techniques. Wastewater treatment and display applications have been studied using prepared nanoparticles. The crystallite size of pristine nanoparticles is 14 nm. Structural and morphological studies have been carried out too [11]. Also, other spinel ferrites were synthesized using the green route with various plant extracts and natural resources like ginger, cardamom, terminalia catappa, clove, egg white, aloe vera, etc. [12]. But no research was found on the synthesis of nickel ferrite nanoparticles using the extract of raw mango pulp. *M. Indica* is a family member of Anacardiaceae with the phylum Magnoliophyta and Magnoliopsida class. Its native is tropical Asia and has been cultivated in the subcontinent of India. The main components of mango are organic acids, sugars, minerals, vitamins, and polyphenols. Mango has biological properties like antioxidants, anti-diabetic, anti-viral, anti-allergic, anti-tumor, anti-HIV, antiparasitic, anti-inflammatory, etc. [13].

In the present study, nickel nanoferrite particles are prepared by green synthesis using raw mango pulp. Structural and elastic properties of synthesized nanoparticles are investigated in the present paper (Table 1).

Materials and Method

Materials

The nickel (II) nitrate hexahydrate [Ni $(NO_3)_2 \cdot 6H_2O$ (M. W. 290.81 g/mol)] and ferric (III) nitrate nonahydrate [$Fe(No_3)_2 \cdot 9H_2O$ (M. W. 404.00 g/mol)] were purchased from Merck. Raw mango is purchased from the local market in Bhavnagar, Gujarat, India.

Preparation of mango pulp

Peeled the raw mango and cut it into small pieces. Further, a juicer was used to crush the raw mango pieces. Mango contains Mg, K, Fe, Cd, Ca, Al, Na, Cu, Zn, Pb, Mn, and ascorbic acid (15.8 - 25.1%) [14] (Figure 1).

Table 1: Summery of introduction.

Extract	Characterization	Application	Crystallite size (nm)	Ref.
Terminalia catappa	XRD, FTIR, FESEM, EDAX, SAED, TEM, and HRTEM	Anticancer activity of breast cancer (MCF-7) cell	8.01 - 11.97	[5]
Ginger	TGA, XRD, FTIR, and UV-VIS	Structural and physical properties	26	[6]
Rosemary extract	XRD, HRTEM, FESEM, XPS, FTIR, EDAX, VSM, TEM, and EDS	Anticancer agent	-	[7]
Clove (*Syzygium aromaticum*)	XRD	Structural study	24 and 26	[8]
S. munja	UV-VIS and FTIR	Production of high yield biofuel	-	[9]
Albumen (egg white)	PXRD, FTIR, EDX, FESEM, and VSM	Physico-chemical properties (physical + chemical)	23 - 47	[10]
Aloe vera	PXRD, SEM, TEM, and HRTEM	Wastewater treatment and display applications	14	[11]
M. Indica pulp (mango)	EDX, SEM, XRD, FTIR, and TEM	Structural and elastic study	This paper	

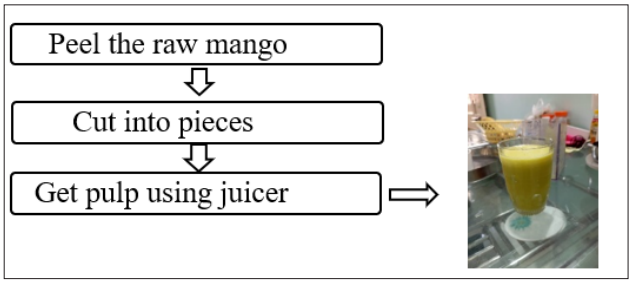


Figure 1: Preparation of mango pulp.

Preparation of $NiFe_2O_4$ nanoparticles

To synthesize nanoparticles using the green synthesis method of $NiFe_2O_4$, 7.27 g of nickel nitrate and 20.2 g of iron nitrate are added into 100 ml of distilled water separately and stirred at 80 °C with 580 revolutions per minute (RPM). Nickel nitrate and iron nitrate are taken in the molar ratio of 1:2 [15]. Nickel nitrate is added to the iron nitrate along with 25 ml of mango pulp, and the mixture is stirred at 80 °C with 230 RPM for 5 h. At the end of the process, a gel-like formation is formed. After some time of stirring, nickel ferrite nanoparticles are formed and put into the furnace for 3 h at 250 °C to make it dry, and it removes humidity. Nickel ferrite powder is sintered at 600 °C in the furnace for 4 h, and we get 6.15 g of nanoparticles of nickel ferrite (Figure 2).

Results and Discussion

EDX analysis

The stoichiometric proportion of nickel ferrite is confirmed by EDX analysis as shown in figure 3. EDX analysis shows that the synthesized nanoparticles consist of the highest nickel, iron, and oxygen elements, and a few peaks of chlorine and potassium are found due to elements being present in the mango pulp [12]. Table 2 shows the comparison between theoretical and experimental molar weight [16].

SEM analysis

Figure 4 shows the surface morphology of the prepared sample. Toxic gases were evaporated during the synthesis process, which creates rough surfaces, voids, and makes nanoparticles pores. Because of combustion, prepared nanoparticles are agglomerated with uniform distribution [17].

XRD analysis

From the XRD graph (Figure 5), it is clear that the prepared material has a cubic spinal structure, and an intense peak shows that the prepared material is highly crystalline, single phase, and has fcc structure with face group fd3m [18]. All the planes are indexing as 111, 220, 311, 222, 400, 422, 333, and 440. The crystallite size is calculated from the intense peak 311 of the XRD graph using Debye-Scherrer's equation 1 [19].

$$D = \frac{k\lambda}{\beta cos\theta} \quad (1)$$

Where, D is crystallite size, k is Scherrer constant = 0.94, λ is the wavelength of the X-ray = 1.54178×10^{-10} m, β is the full width at half maximum = 0.01797 radian, and cosθ is cos(0.3132) = 0.95134.

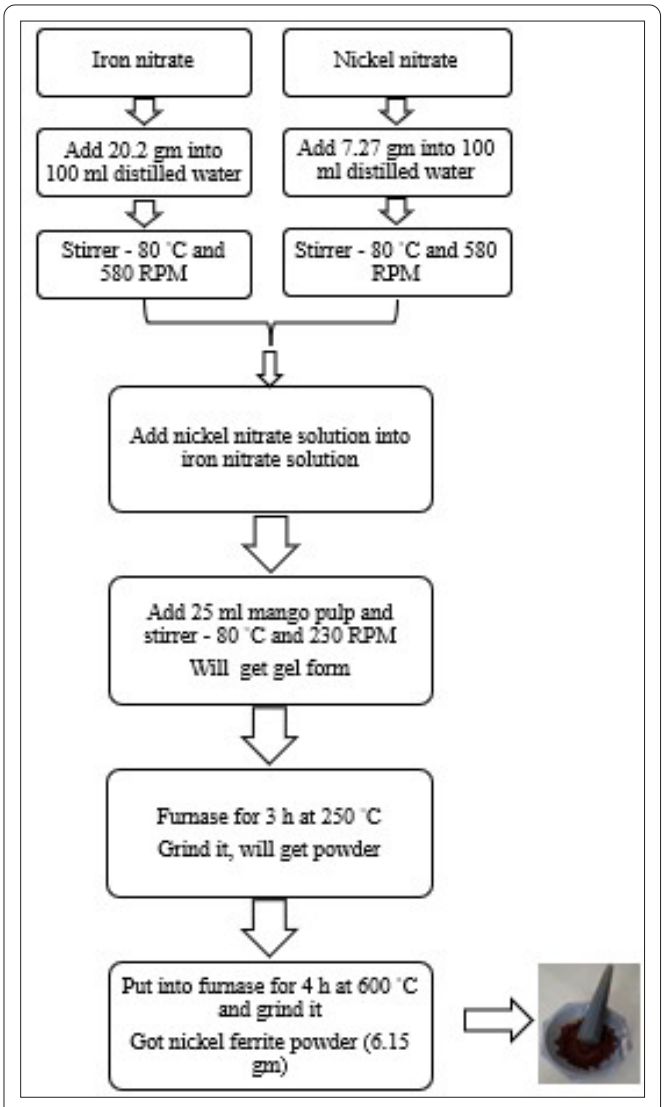


Figure 2: Preparation of nickel ferrite nanoparticles.

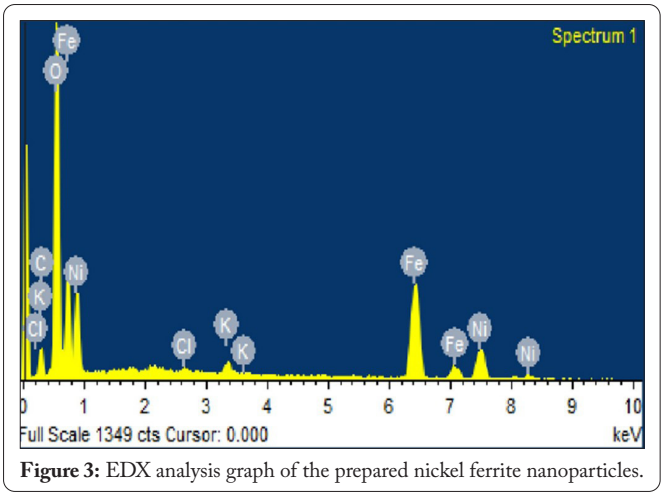


Figure 3: EDX analysis graph of the prepared nickel ferrite nanoparticles.

X-ray density refers to electrons within the crystal, and deeply bound electrons show how the crystal diffracts X-rays.

$$\rho_{x-ray} = \frac{8M_W}{N_A a^3} \quad (2)$$

Where, px-ray = X-ray density = 5.445 $\frac{gm}{cm^3}$, M_W is molecular

Table 2: Comparison between theoretical and experimental molar weight in % of synthesized specimen.

Element	Molar weight (g/mol)	Total molar weight (g/mol)	Moler weight in % (Theoretically)	Moler weight in % (Experimentally)
Nickel	58.693	58.693	25.04	22.73
Iron	55.845	111.69	47.65	42.59
Oxygen	15.999	63.996	27.3	34.67
$NiFe_2O_4$	-	234.38	99.99	99.99

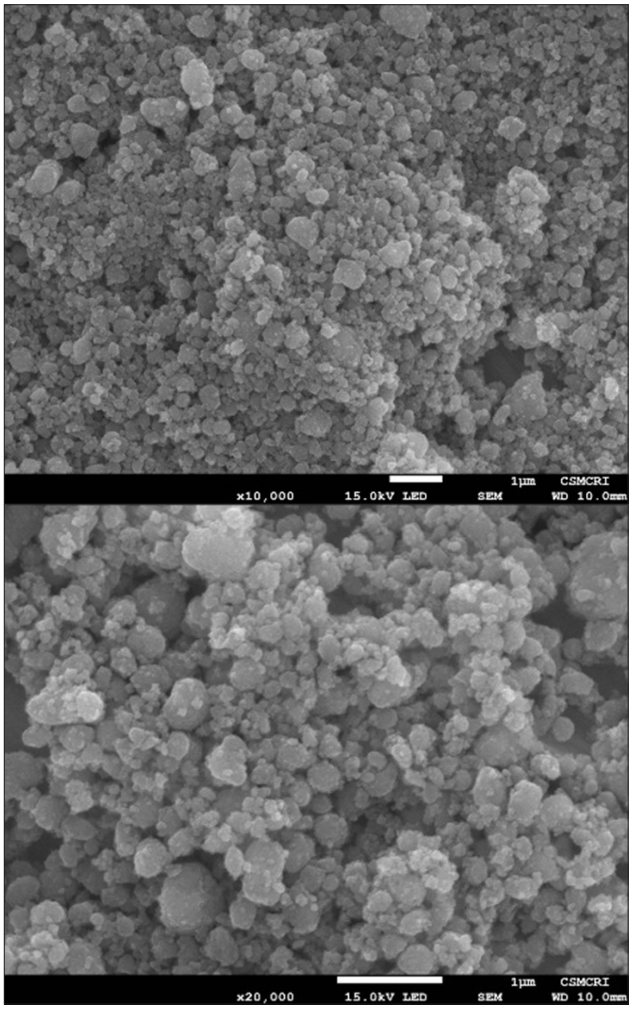


Figure 4: SEM of synthesized specimen.

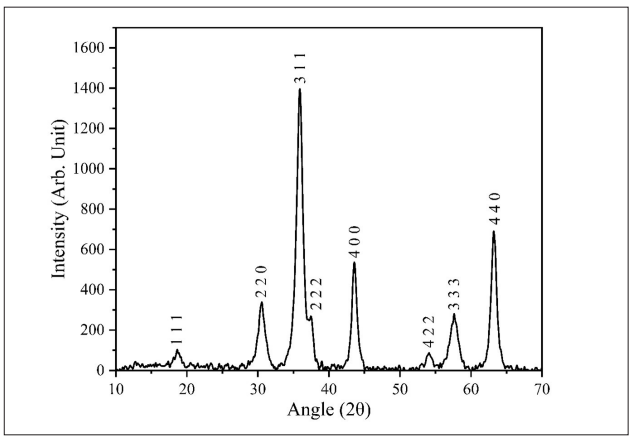


Figure 5: XRD of synthesized specimen.

weight = 234.38 $\frac{gm}{mol}$, N_A is Avogadro's number = 6.023 × 10^{23} $\frac{atoms}{mol}$, and a is Lattice constant = 8.2995 × 10^{-8} cm.

Bulk density is mass per unit volume, which shows how closely or tightly atoms are bound together.

$$\rho_{bulk} = \frac{m}{\pi r^2 t} \quad (3)$$

Where, ρ_{bulk} is bulk density, m is the mass of pellet = 0.337 gm, r is the radius of pellet = 1 cm, and t is the thickness of pellet = 0.19 cm.

Porosity is the empty space or voids within the crystal structure, which is calculated using the formula (4).

$$P = \frac{\rho_{x-ray} - \rho_{bulk}}{\rho_{x-ray}} \times 100 \quad (4)$$

Surface area is calculated from equation 5:

$$S = \frac{6000}{\rho_{x-ray} \times D} \quad (5)$$

Dislocation density is calculated using equation 6:

$$\delta = \frac{1}{D^2} \quad (6)$$

From equations 1 - 6, various structural properties are calculated, which are shown in table 3 [18-20].

Furthermore, cation distribution for nickel ferrite is $(NI_{0.05}^{2+}Fe_{0.95}^{3+})_A (NI_{0.95}^{2+} Fe_{1.05}^{3+})_B O_4^{2-}$ [21, 22]. Fe^{+2} occupies the A site while Ni^{2+} and Fe^{3+} occupy the B site. The ionic radius of the tetrahedral site is r_A, and for octahedral sites is r_B, which is calculated using equations 7 and 8.

$$r_A = (C_{ANi^{2+}}) \cdot r(Ni^{2+}) + (C_{AFe^{3+}}) \cdot r(Fe^{3+}) \quad (7)$$

$$r_B = (C_{BNi^{2+}}) \cdot r(Ni^{2+}) + (C_{BFe^{3+}}) \cdot r(Fe^{3+}) \quad (8)$$

Where, $r(Ni^{2+})$ is 0.69Å, $r(Fe^{3+})$ is 0.64Å, $(C_{ANi^{2+}})$ and $(C_{AFe^{3+}})$ are the concentration on the A site of Ni^{2+} and Fe^{3+}, respectively, and $(C_{BNi^{2+}})$ and $(C_{BFe^{3+}})$ are the concentration on the B site of Ni^{2+} and Fe^{3+}, respectively. Moreover, the comparison between ionic radii (r_A and r_B) and site radii (R_A and R_B) took place.

Also, the lattice parameter is proportional to the ionic radius, and the theoretical value of the lattice parameter can be calculated using equation 9.

$$a_{th} = \frac{8}{\sqrt[3]{3}} \left[(r_A + R_0) + \sqrt{3}(r_B + R_0) \right] \quad (9)$$

Where, R_0 is radius of oxygen ion = 1.32Å.

Table 3: Structural parameters from XRD analysis-1.

Physical quantity	Value
Crystalline size (nm)	8.4774
X-ray density $\left(\frac{gm}{cm^3}\right)$	5.445
Bulk density $\left(\frac{gm}{cm^3}\right)$	2.26
Porosity (%)	58.49
Surface area $\left(\frac{cm^2}{gm}\right)$	1.229×10^{11}
Dislocation density (m^{-2})	1.391×10^{16}

The value of experimental lattice parameter a_{exp} is a good match with the theoretical value a_{th} [23]. In spinel ferrite, the hopping length is the distance between the magnetic ions. For the tetrahedral sites, the hopping length is L_A, and for the octahedral sites, the hopping length is L_B, which can be derived using equations 10 and 11.

$$L_A = \frac{a\sqrt{3}}{4} \tag{10}$$

$$L_B = \frac{a\sqrt{2}}{4} \tag{11}$$

Therefore, from equations 10 and 11, we can say that, with an increase in ionic radius, the hopping length is also increased [24]. The distance between the face of the cube edge along the cube diagonal of the spinel lattice and an anion (oxygen ion) is called the anion parameter (oxygen positional parameter). The anion parameter for a tetrahedral site is u^{43m}, and for an octahedral site is u^{3m}. To calculate u^{3m} and u^{43m} equations 12 and 13 can be used.

$$u^{3m} = \frac{\frac{1}{4}R^2 - \frac{2}{3} + \left(\frac{11}{48}R^2 - \frac{1}{18}R^2\right)^{\frac{1}{2}}}{2R^2 - 2} \tag{12}$$

$$u^{43m} = \frac{\frac{1}{2}R^2 - \frac{11}{12} + \left(\frac{11}{48}R^2 - \frac{1}{18}R^2\right)^{\frac{1}{2}}}{2R^2 - 2} \tag{13}$$

Where, $R = \frac{B-O}{A-O}$, B - O and A - O are the average bond lengths, which can be described using the cation distribution. A - O = $\langle r_A + R_0 \rangle$ and B - O = $\langle r_B + R_0 \rangle$. Equation 12 gives the anion parameter by assuming that the center of symmetry (origin at B site) is at $\left(\frac{1}{4},\frac{1}{4},\frac{1}{4}\right)$, for which u_{ideal} is 0.250 Å. Similarly, for equation 13, assuming that the center of symmetry (origin at A site) at $\left(\frac{3}{8},\frac{3}{8},\frac{3}{8}\right)$, for which u_{ideal} is 0.375Å. To convert the origin from A site to B site, $u^{43m} = \left(u^{3m} + \frac{1}{8}\right)$ relation can be used [20, 25]. Moreover, the site radii R_A and R_B can be compared with the ionic radii r_A and r_B.

$$R_A = \left(u^{43m} - 0.25\right)a\sqrt{3} - R_0 \tag{14}$$

$$R_B = \left(0.625 - u^{43m}\right)a - R_0 \tag{15}$$

By using the value of experimental lattice parameter a_{exp} and anion positional parameter u^{43m} the octahedral bond length(d_{BX}), tetrahedral bond length(d_{AX}), shared octahedral edge length(d_{BEX}), shared tetrahedral edge length(d_{AEX}), and unshared octahedral edge length(d_{BEXU}) are calculated using equations 16 - 20 [20, 25].

$$d_{AX} = a\sqrt{3}\left(u - \frac{1}{4}\right) \tag{16}$$

$$d_{BX} = a\left[3u^2 - \left(\frac{11}{4}\right)u - \left(\frac{43}{64}\right)\right]^{\frac{1}{2}} \tag{17}$$

$$d_{AEX} = a\sqrt{2}\left(2u - \frac{1}{2}\right) \tag{18}$$

$$d_{BEX} = a\sqrt{2}\left(1 - 2u\right) \tag{19}$$

$$d_{BEXU} = a\left[4u^2 - 3u - \left(\frac{11}{16}\right)\right]^{\frac{1}{2}} \tag{20}$$

Ionic radii r_A and r_B from equations 7 and 8, respectively, lattice parameter a_{th} from equation 9, hopping length L_A and L_B from equations 10 and 11, respectively, anion parameter u^{3m} and u^{43m} from equation 12 and 13, respectively, site radii R_A and R_B from equations 14 and 15, respectively, and d_{AX}, d_{BX}, d_{AEX}, d_{BEX}, d_{BEXU} from equations 16 - 20, respectively are calculated for the prepared specimen and the final values are shown in the table 4.

Table 4: Structural parameters from XRD analysis-2.

Physical quantity	Values (nm)
The ionic radius of tetrahedral site rA	0.0642
The ionic radius of octahedral site r_B	0.0664
Lattice constant a_{th}	0.8311
Lattice constant a_{exp}	0.8299
Hopping length for tetrahedral site L_A	0.3594
Hopping length for tetrahedral site L_B	0.2934
Anion (oxygen) positional parameter u^{3m}	0.0261
Anion (oxygen) positional parameter u^{43m}	0.0386
Tetrahedral site radius R_A	0.0643
Octahedral site radii R_B	0.0659
Tetrahedral bond length(d_{AX})	0.1963
Octahedral bond length(d_{BX})	0.1984
Shared tetrahedral edge length(d_{AEX})	0.3205
Shared octahedral edge length(d_{BEX})	0.2664
Unshared octahedral edge length(d_{BEXU})	0.294

The interionic distances between cations Me - Me (i.e., b, c, d, e, f) can be calculated using equations 21 - 25, from equations we can say that, as the lattice parameter increased the distance between cations (distance between metal ions) is also increased.

$$b = \frac{a}{4}\sqrt{2} \tag{21}$$

$$c = \frac{a}{8}\sqrt{11} \quad (22)$$

$$d = \frac{a}{4}\sqrt{3} \quad (23)$$

$$e = \frac{3a}{8}\sqrt{3} \quad (24)$$

$$f = \frac{a}{4}\sqrt{6} \quad (25)$$

Interionic distances between cation-anion Me – MO (i.e., p, q, r, and s) are calculated using equations 26 - 29, which are shown in table 5 and table 6.

$$p = a\left(\frac{1}{2} - u^{3m}\right) \quad (26)$$

$$q = a\left(u^{3m} - \frac{1}{8}\right)\sqrt{3} \quad (27)$$

$$r = a\left(u^{3m} - \frac{1}{8}\right)\sqrt{11} \quad (28)$$

$$s = \frac{a}{3}\left(u^{3m} + \frac{1}{2}\right)\sqrt{3} \quad (29)$$

Table 5: Interionic distances between cations (Me - Me).

Bond length	Values (nm)
b	0.2934
c	0.3441
d	0.3594
e	0.5391
f	0.5082

Table 6: Interionic distances between cations and anions (Me - MO).

Bond length	Values (nm)
p	0.1979
q	0.1962
r	0.3758
s	0.3649

Moreover, bond angles between the A sites, between the B sites, and between the A - B sites are calculated using equations 30 - 34, which are inverse cosine functions of trigonometry (Figure 6). Values for the prepared nickel ferrite nanoparticles are shown in table 7 [20, 26].

$$\theta_1 = cos^{-1}\left[\frac{p^2 + q^2 - c^2}{2pq}\right] \quad (30)$$

$$\theta_2 = cos^{-1}\left[\frac{p^2 + r^2 - e^2}{2pr}\right] \quad (31)$$

$$\theta_3 = cos^{-1}\left[\frac{2p^2 - b^2}{2p^2}\right] \quad (32)$$

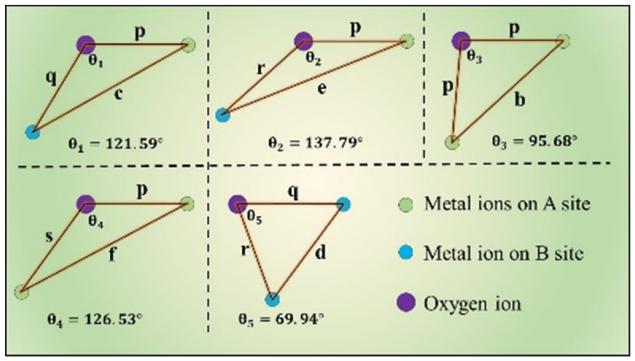


Figure 6: Bond angles and interionic distances between A sites, B sites, and A-B sites of synthesized specimen.

Table 7: Bond angles between A sites, B sites, and A-B sites.

Interionic angels	Values (degree)
θ_1	121.59
θ_2	137.79
θ_3	95.68
θ_4	126.53
θ_5	69.94

$$\theta_4 = cos^{-1}\left[\frac{p^2 + s^2 - f^2}{2ps}\right] \quad (33)$$

$$\theta_5 = cos^{-1}\left[\frac{r^2 + q^2 - d^2}{2rq}\right] \quad (34)$$

FTIR analysis

From the FTIR, information about the position and occupation of the ions in the spinel ferrites can be derived. Waldron's classification states that there are always two broad metal oxygen absorption bands present in the infrared spectra [27, 28].

In figure 7, absorption peaks 405.94 cm^{-1} and 548.64 cm^{-1} represent the tetrahedral metal oxygen ions and octahedral metal oxygen ions vibrations, respectively. The force constants for tetrahedral and octahedral sites are K_t and K_0 respectively,

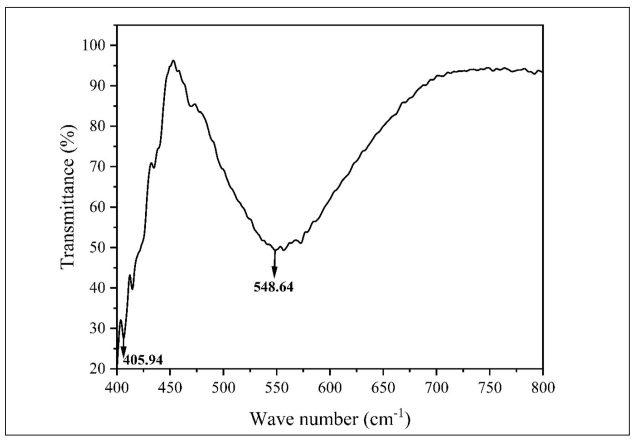


Figure 7: FTIR spectra of synthesized specimen.

which are calculated using equations 35 and 26 for the prepared specimen sample [28].

$$K_t = 7.62 \times M_1 \times \vartheta_1^2 \times 10^{-7}\, N/m \quad (35)$$

$$K_0 = 10.62 \times \frac{M_2}{2} \times \vartheta_2^2 \times 10^{-7}\, N/m \quad (36)$$

Where, molecular weight on A site and B site, can be represented as M_1 and M_2, respectively. The value of M_1 and M_2 can be calculated using equations 37 and 38.

$$M_1 = C_{ANi^{2+}} \times M_{Ni} + C_{AFe^{3+}} \times M_{Fe} \quad (37)$$

$$M_2 = C_{BNi^{2+}} \times M_{Ni} + C_{BFe^{3+}} \times M_{Fe} \quad (38)$$

Moreover, the stiffness constant (C_{11} and C_{12}) can be determined using the relation,

$$Longitudinal\ modulus = C_{11} = L = \frac{K_{avg}}{a} \quad (39)$$

Where, K_{avg} is the mathematical average ($K_{avg} = \frac{K_t + K_0}{2}$) of force constant K_t and K_0, and a is the lattice constant.

$$Stiffness\ constant = C_{12} = \frac{\sigma C_{11}}{(1-\sigma)} \quad (40)$$

Where, σ is the Poisson ratio, which can be written as equation 41.

$$\sigma = 0.324(1 - 1.043 f) \quad (41)$$

Where, f is the pore fraction, for prepared nickel ferrite nanoparticles; pore fraction is 0.5849 and Poisson's ratio (σ) is 0.126.

Using equations 40 and 41, elastic properties like Young's modulus (E), Rigidity modulus (G), and Bulk modulus (K) are also calculated [29, 30]. Such calculations are done using the cation distribution and from the absorption wavelength [20, 31].

$$E = \frac{(C_{11} - C_{12})(C_{11} + 2C_{12})}{C_{11} + C_{12}} \quad (42)$$

$$G = \frac{E}{2(\sigma + 1)} \quad (43)$$

$$K = \frac{1}{3}[(C_{11} + 2C_{12})] = L - \frac{4}{3}G \quad (44)$$

Calculated values of force constant and elastic parameters are shown in table 8.

Table 8: Force constant and elastic parameters of synthesized specimen.

Physical quantity	Values
Molecular weight on A site (kg)	55.99 × 10^{-3}
Molecular weight on B site (kg)	114.40 × 10^{-3}
Force constant for tetrahedral site (N/m)	128.41
Force constant for octahedral site (N/m)	100.09
Stiffness constant (GPa)	19.9
Young's modulus (E) (GPa)	132
Rigidity modulus (G) (GPa)	58.8
Bulk modulus (K) (GPa)	59.1

TEM analysis

Figure 8 shows the TEM image of synthesized nickel ferrite nanoparticles. The particle size of prepared nanoparticles is 9.865 nm, which is calculated using the ImageJ software. Figure 9 shows the histogram of particle size and is also fitted by the Gaussian distribution function derived from the TEM measurement [32].

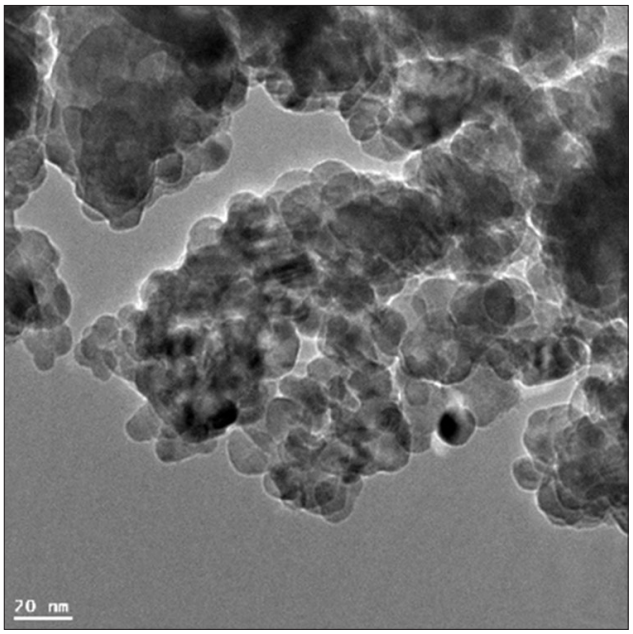


Figure 8: TEM image of synthesized specimen.

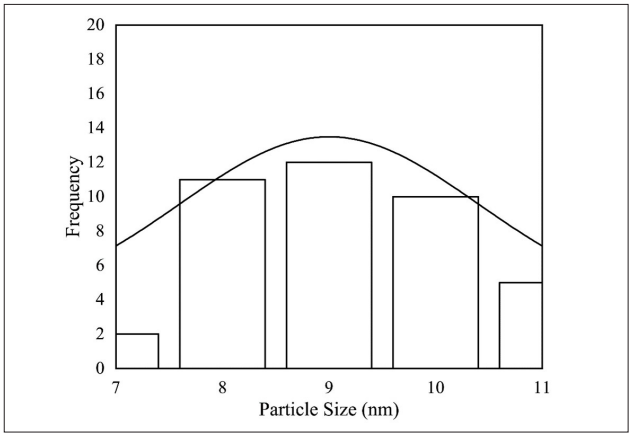


Figure 9: Histogram of particle size using TEM.

Conclusion

Nickel ferrite nanoparticles are successfully synthesized using the green synthesis method. The elemental stoichiometry was confirmed by the EDX analysis, and it also confirms that the prepared nanoparticles have no impurity. SEM suggests that nanoparticles are agglomerated, have pores, and have rough surfaces. The XRD analysis reveals that the prepared specimen has a spinel structure. Moreover, the cubic spinel structure of prepared nanoparticles belongs to the fd3m space group, which is confirmed by the XRD analysis. Structural parameters like crystallite size, X-ray density, bulk density, sur-

face area, porosity, ionic radii, anion parameter, hopping length, and shared and unshared edge length of interatomic distances were calculated using the XRD analysis for nanoparticles. Two absorption wavelengths have been observed in the FTIR spectra. From the FTIR, tetrahedral and octahedral force constants are calculated, which are 128.41 N/m and 100.09 N/m, respectively. Furthermore, stiffness constant, Young's modulus, rigidity modulus, and bulk modulus are found in the order of GPa. Which shows that the synthesized material is rigid and resists deforming. The particle size of nickel ferrite nanoparticle is about ~10 nm has been drawn from TEM analysis.

Acknowledgements

Authors are thankful to RK University and Maharaja Krishnakumarsinhji Bhavnagar University for providing well-equipped laboratory facilities. This paper was presented at the 2nd International Conference on Innovations in Molecular Structure Instrumental Approaches (ICMSI 2025), sponsored by Royal Society of Chemistry, UK and Council of Scientific & Industrial Research, India on 7th and 8th April 2025, organized by the School of Science, RK University, Rajkot, Gujarat, India.

Conflict of Interest

None.

References

1. Dhiman P, Rana G, Goyal D, Goyal A. 2021. Basics of Ferrites: Types and Structures. In Bhargava GK, Bhardwaj S, Singh M, Batoo KM (eds) Ferrites and Multiferroics. Engineering Materials. Springer, Singapore, pp 1–25.
2. Desai HB, Tanna AR. 2021. Effect of Substitution on the Electric and Magnetic Properties of Ferrites. In Bhargava GK, Bhardwaj S, Singh M, Batoo KM (eds) Ferrites and Multiferroics. Engineering Materials. Springer, Singapore, pp 49–69.
3. Tilley RJ. 2020. Crystals and Crystal Structures. John Wiley & Sons.
4. O'Neill HSC, Navrotsky A. 1983. Simple spinels; crystallographic parameters, cation radii, lattice energies, and cation distribution. *Am Mineral* 68(1-2): 181–194.
5. Sarala E, Vinuth M, Praveen BM, Chandrappa CP, Shivakumara C, et al. 2022. Green synthesis of nickel ferrite nanoparticles using *Terminalia catappa*: structural, magnetic and anticancer studies against MCF-7 cell lines. *J Hazard Mater Adv* 8: 100150. https://doi.org/10.1016/j.hazadv.2022.100150
6. Patil SV, Kshirsagar SD, Patil PS, Shinde NM, Mane RG, et al. 2020. Synthesis of nanocrystalline nickel ferrite through soft chemistry method: a green chemistry approach using ginger extract. *AIP Conf Proc* 2265(1): 030178. https://doi.org/10.1063/5.0017071
7. Alijani HQ, Pourseyedi S, Shahbazi-Gahrouei D, Hashemzadeh A, Ghafarzadegan R, et al. 2020. Bimetallic nickel-ferrite nanorod particles: greener synthesis using rosemary and its biomedical efficiency. *Artif Cells Nanomed Biotechnol* 48(1): 242–251. https://doi.org/10.1080/21691401.2019.1699830
8. Kulkarni GD, Patade SR, Gaikwad PP, Patil SP, Khot VS, et al. 2020. Green synthesis of $NiFe_2O_4$ nanoparticles using different fuels and their structural characterization. *J Phys Conf Ser* 1644(1): 012003. https://doi.org/10.1088/1742-6596/1644/1/012003
9. Din MI, Javed M, Khalid R, Hussain Z, Shafique M, et al. 2020. Slow catalytic pyrolysis of *Saccharum munja* using bio-genically synthesized nickel ferrite nanoparticles for the production of high yield biofuel. *Eur J Sustain Dev Res* 4(3): 1-9. https://doi.org/10.29333/ejosdr/7900
10. Udhaya PA, Meena M. 2019. Albumen assisted green synthesis of $NiFe_2O_4$ nanoparticles and their physico-chemical properties. *Mater Today Proc* 9(3): 528–534. https://doi.org/10.1016/j.matpr.2018.10.372
11. Nadumane A, Shetty AN, Nandibewoor ST, Vasantharaju SG, Bhatt AS, et al. 2019. Sunlight photocatalytic performance of Mg-doped nickel ferrite synthesized by a green sol–gel route. *J Sci Adv Mater Devices* 4(1): 89–100. https://doi.org/10.1016/j.jsamd.2018.12.002
12. Chaudhari A, Kaida T, Desai HB, Ghosh S, Bhatt RP, et al. 2022. Dye degradation and antimicrobial applications of manganese ferrite nanoparticles synthesized by plant extracts. *Chem Phys Impact* 5: 100098. https://doi.org/10.1016/j.chphi.2022.100098
13. Shah KA, Patel MB, Patel RJ, Parmar PK. 2010. *Mangifera indica* (mango). *Pharmacogn Rev* 4(7): 42-48. https://doi.org/10.4103/0973-7847.65325
14. Othman OC, Mbogo GP. 2009. Physico-chemical characteristics of storage-ripened mango (*Mangifera indica* L.) fruits varieties of eastern Tanzania. *Tanzan J Sci* 35: 57-65.
15. Sutka A, Mezinskis G. 2012. Sol-gel auto-combustion synthesis of spinel-type ferrite nanomaterials. *Front Mater Sci* 6: 128–141. https://doi.org/10.1007/s11706-012-0167-3
16. Manju BG, Raji P. 2020. Green synthesis, characterization, and antibacterial activity of lime-juice-mediated copper–nickel mixed ferrite nanoparticles. *Appl Phys A* 126(3): 156. https://doi.org/10.1007/s00339-020-3313-2
17. Naik MM, Vinuth M, Kumar VU, Hemakumar KH, Preethi G, et al. 2023. A facile green synthesis of nickel ferrite nanoparticles using *Tamarindus indica* seeds for magnetic and photocatalytic studies. *Nanotechnol Environ Eng* 8(1): 143–151. https://doi.org/10.1007/s41204-022-00257-x
18. Anantharamaiah PN, Rao P, Shashanka HM, Khopkar V, Chelvane JA, et al. 2022. Tunable dielectric properties of nickel ferrite derived via crystallographic site preferential cation substitution. *J Phys Chem C* 126(21): 9123–9134. https://doi.org/10.1021/acs.jpcc.2c00529
19. Hathiya LJ, Tanna AR, Baraliya JD, Joshi HH. 2020. Study of ternary nano-structured ferrite $Mn_{0.6}Co_{0.2}Ni_{0.2}Fe_2O_4$ for its magnetic and chemical dye degradation properties. *AIP Conf Proc* 2220: 020155. https://doi.org/10.1063/5.0001742
20. Hathiya LJ, Baraliya JD, Jethva HO, Joshi HH. 2022. Structural, dielectric and ac electrical properties of nano-structured $Mn_{0.6}Co_{0.2}Ni_{0.2}Fe_2O_4$ ternary ferrite synthesized by citrate-gel auto-combustion technique. *Indian J Pure Appl Phys* 60(1): 59–71. https://doi.org/10.56042/ijpap.v60i1.54818
21. Desai HB, Kumar A, Tanna AR. 2021. Structural and magnetic properties of $MgFe_2O_4$ ferrite nanoparticles synthesis through auto combustion technique. *Eur Chem Bull* 10(3): 186–190.
22. Tanna AR, Joshi HH. 2013. Computer aided X-ray diffraction intensity analysis for spinels: hands-on computing experience. *Proc World Acad Sci Eng Technol* 7(3): 334-341.
23. Hakim MA, Nath SK, Sikder SS, Maria KH. 2013. Cation distribution and electromagnetic properties of spinel type Ni–Cd ferrites. *J Phys Chem Solids* 74(9): 1316–1321. https://doi.org/10.1016/j.jpcs.2013.04.011
24. Batoo KM, Kumar G, Yang Y, Al-Douri Y, Singh M, et al. 2017. Structural, morphological and electrical properties of Cd^{2+} doped $Mg-Fe_{2-x}O_4$ ferrite nanoparticles. *J Alloys Compd* 726: 179–186. https://doi.org/10.1016/j.jallcom.2017.07.237
25. Lakhani VK, Pathak TK, Vasoya NH, Modi KB. 2011. Structural parameters and X-ray Debye temperature determination study on copper-ferrite-aluminates. *Solid State Sci* 13(3): 539–547. https://doi.org/10.1016/j.solidstatesciences.2010.12.023
26. Debnath S, Das A, Das R. 2021. Effect of cobalt doping on structural parameters, cation distribution and magnetic properties of nickel ferrite nanocrystals. *Ceram Int* 47(12): 16467–16482. https://doi.org/10.1016/j.ceramint.2021.02.095

27. Abdellatif MH, Azab AA. 2019. Elastic properties of Cr-doped Mn ferrite. *Bull Natl Res Cent* 43: 1–8. https://doi.org/10.1186/s42269-019-0143-5

28. Waldron RD. 1955. Infrared spectra of ferrites. *Phys Rev J Arch* 99(6): 1727. https://doi.org/10.1103/PhysRev.99.1727

29. Babu BR, Tatarchuk T. 2018. Elastic properties and antistructural modeling for nickel-zinc ferrite-aluminates. *Mater Chem Phys* 207: 534–541. https://doi.org/10.1016/j.matchemphys.2017.12.084

30. Manash A, Kumar R, Kumar R, Pandey SC, Kumar S. 2022. Elastic properties of ferrite nanomaterials: a compilation and a review. *Int Res J Adv Sci Hub* 4(12): 312–317.

31. Bhatu SS, Lakhani VK, Tanna AR, Vasoya NH, Buch JU, et al. 2007. Effect of nickel substitution on structural, infrared and elastic properties of lithium ferrite. *Indian J Pure Appl Phys* 45(7): 596-608.

32. Desai HB, Hathiya LJ, Joshi HH, Tanna AR. 2020. Synthesis and characterization of photocatalytic $MnFe_2O_4$ nanoparticles. *Mater Today Proc* 21(4): 1905-1910. https://doi.org/10.1016/j.matpr.2020.01.248